Nanoscale

Understanding and Controlling the Depth Sensitivity of Scanning Probe Based Infrared Imaging and Nanospectroscopy for Buried Polymeric Structures

Journal:	*Nanoscale*
Manuscript ID	NR-ART-04-2023-001657.R1
Article Type:	Paper
Date Submitted by the Author:	03-May-2023
Complete List of Authors:	Prine, Nathaniel; University of Southern Mississippi, School of Polymer Science and Engineering Cardinal, Camille; University of Southern Mississippi, School of Polymer Science and Engineering Gu, Xiaodan; University of Southern Mississippi, School of Polymer Science and Engineering

SCHOLARONE™
Manuscripts

Understanding and Controlling the Depth Sensitivity of Scanning Probe Based Infrared Imaging and Nanospectroscopy for Buried Polymeric Structures

*Nathaniel Prine, Camille Cardinal, Xiaodan Gu**

School of Polymer Science and Engineering, Center for Optoelectronic Materials and Devices,

The University of Southern Mississippi, Hattiesburg, MS 39406, USA.

Correspondence to: Xiaodan Gu. *E-mail: xiaodan.gu@usm.edu*

Key Words: Scanning probe microscopy, infrared spectroscopy, thin-film morphology characterization, depth sensitivity, phase behavior, composites.

ABSTRACT

Atomic force microscopy paired with infrared spectroscopy (AFM-IR) is a robust technique for interrogating complex polymer blends and composites' nanoscale surface topography and chemical composition. In this work, we measured bilayer polymer films to study the effect of laser power, laser pulse frequency, and laser pulse width on the depth sensitivity of the technique. Unique bilayer polystyrene (PS) and polylactic acid (PLA) samples with varied film thickness and blend ratios were prepared. The depth sensitivity characterized by the amplitude ratio of the resonance bands of PLA and PS was monitored as the thickness of the top barrier layer was incrementally increased from tens of nanometers to hundreds of nanometers. In addition, incrementally increasing the incident laser power resulted in greater depth sensitivity due to the enhanced thermal oscillations generated in the buried layer. In contrast, incrementally increasing the laser frequency increased surface sensitivity, as indicated by a reduced PLA/PS AFM-IR signal ratio. Lastly, a dependence of the depth sensitivity on laser pulse width was observed. Consequently, by precisely controlling the laser energy, pulse frequency, and pulse width, one can finely control the depth sensitivity of the AFM-IR tool from 10 nm to 100 nm. Our work provides the unique capability to study buried polymeric structures without the need for tomography or destructive etching.

INTRODUCTION

The future of material design relies on rapidly assessing material properties such as chemical composition, crystallinity, and surface morphology at the nanoscale. Notably, as

technology compacts towards the nanoscale, the morphology of polymer blends, nanocomposites, and multilayer films grows more complex with each decade.[1,2] With this in mind, simultaneously observing the surface and volume morphology is critical to advances in the life and material sciences.[3,4] The ability to observe subsurface features at the nanoscale, otherwise known as nanotomography, is valuable for gaining a holistic understanding of multicomponent systems and their interactions. Polymer blends and copolymers are integral to consumer goods,[5,6] energy applications,[7–9] and medical devices[5,10,11] because their properties can be tuned by controlling the blend ratio or stoichiometry of components. Interestingly, the surface morphology of these systems differs significantly from the bulk[12–14] and requires the use of both volume-based and surface-based characterization tools to gain a complete comprehension of the system. Additionally, understanding the morphology near the interface is crucial for polymer coating,[15,16] bioelectronics,[17–20] electrode/electrolyte interfaces.[21,22]

Non-destructive methods for characterizing the subsurface morphology of materials remain limited.[23] Originally, optical microscopy was used to investigate subsurface features, but these techniques remain limited by the diffraction of light and lack the resolution required to measure nanoscale features.[24,25] Both scanning electron microscopy (SEM) and transmission electron microscopy (TEM) have been used in nanotomography with impressive resolution down to the nanometer range or lower, despite complicated sample preparation.[26–28] However, their contrast mechanism, which relies on differences in electron density, limits the scope of soft material composites that can be measured and results in poor contrast.[25,26,29,30] Electron energy loss spectroscopy (EELS) is a technique that uses a transmission electron microscope (TEM) to measure the energy losses of electrons as they interact with a sample, providing information about the sample's composition and bonding. EELS has been used for the characterization of polymers,

including cross-linked networks, and has been shown to provide sub-nanometer resolution. EELS can be used to analyze the subsurface morphology of materials without causing damage to the sample, making it a non-destructive technique.[31,32] Additionally, it can provide information about the spatial distribution of elements within the sample, including those present in trace amounts. However, the sample preparation for EELS can be time-consuming and requires high-cost, specialized equipment and expertise, which limits its applicability in some cases.[32] Another limitation of EELS is that the technique is sensitive to the electron dose used during the measurements. A high electron dose can cause radiation damage to the sample, leading to alterations in the chemical composition and morphology of the material. Therefore, the acquisition time and electron dose used during EELS measurements must be carefully controlled to avoid radiation damage to the sample. In addition, EELS measurements can suffer from background noise, which can limit the sensitivity and accuracy of the technique.[31,32] The noise can arise from various sources, including stray electrons and plasmon excitations, and can interfere with the accurate measurement of the sample's composition and morphology.[32] Depth profiling by X-ray photoelectron spectroscopy (XPS) is another technique used for nanotomography; however, its use has a few limitations. First, depth profiling by XPS uses an ion beam to sputter away the top layer for data collection at different depths, classifying it as a destructive technique.[33] Second, the rate at which the ion beam etches away material from the surface changes depending on the material, which would produce inaccurate depth values for multicomponent films.[25,34] Lastly, XPS measures composition only in the Z- direction and suffers from little to no resolution in the lateral direction, as determined by the X-ray beam size. In short, current spectroscopic techniques are poorly suited for measuring vertical chemical and morphological variance in the Z-direction within thin-film polymer structures.

Notably, significant contributions have been made in X-ray tomography, where techniques such as resonant soft X-ray scattering (RSoXS), scanning transmission X-ray microscopy (STXM), and ptychography have been used to resolve the domain interfaces and interphases in bulk heterojunction morphologies.[27,35] In the case of X-ray scattering, real-space imaging of the sample cannot be directly accessed due to the lack of the scattered phase in the measured signal. For this reason, X-ray techniques only provide partial pieces of information about a sample and supporting morphological information using other methods is often necessary.[36] In the case of STXM, particles on the order of ~40 nm can be resolved; however, successfully measuring samples with thicknesses on the order of nanometers is a challenge without causing radiation damage to the film.[27,37] Lastly, while ptychography can achieve a resolution down to 10 nm, this has only been accomplished using radiation-resistant samples or a combination of using soft X-ray energies and cryogenic sample temperatures.[27,38,39]

Previous reports detail tomographic measurements made using AFM by modeling the probe-sample interactions in terms of the tip force applied to the surface and the degree of energy dissipation of the sample.[40,41] Multi-modal AFM imaging such as DC-based, amplitude-modulated AFM, and Kelvin probe force microscopy (KPFM) have also demonstrated the ability to access subsurface features.[42] Cui and coworkers used KPFM to analyze the bulk heterojunction morphology of an all-polymer solar cell at both the top and bottom surface.[43] While impressive, neither depth profiling nor visual imaging of the underlayer were acquired, and analysis was limited to 1-D plots of contact potential difference as a function of scan size. Infrared-based SPM techniques such as atomic force microscopy paired with infrared microscopy (AFM-IR) have shown to be useful for nanotomography and offer the ability to measure chemical composition as

a function of topography.[25,44] However, there is no work demonstrating facile control over the probing depth of AFM-IR.

Promising nanotomography techniques in scanning probe microscopy (SPM) measure cantilever responses due to external stimuli applied through the sample in the form of monochromatic light or oscillating mechanical stress.[25] Traditional atomic force microscopy (AFM) is an SPM technique that produces contrast between two materials because of their difference in elasticity and topography. However, AFM alone is a surface-sensitive technique and cannot detect underlying structures if they do not produce a noticeable effect at the interface of the sample and probe. Among SPM techniques, AFM-IR is the most promising for detecting subsurface features due to the nature of its contrast mechanism, which relies on differences in infrared absorption bands. The technique entails rastering an AFM probe across the sample surface while simultaneously irradiating the sample with a pulsed, tunable infrared laser.[45] The AFM-IR detects the absorption of infrared light through the change in probe height in response to rapid thermal expansion occurring beneath the probe. Typically represented as solely a surface characterization technique, AFM-IR demonstrates, in this study, high sensitivity to underlying structures with unique infrared absorption properties. Although AFM-IR shows excellent potential as a robust tool for nanotomography, no studies have demonstrated facile control of the depth of characterization of AFM-IR without the use of embedded materials, which their topographical and mechanical properties can distinguish.

Herein, the factors contributing to the depth of characterization of AFM-IR are investigated. For the first time, control over the depth of probe of AFM-IR is demonstrated using both spectroscopy and direct infrared imaging of buried microstructure and domains. We studied the effect of various infrared laser parameters to systematically understand how to control the

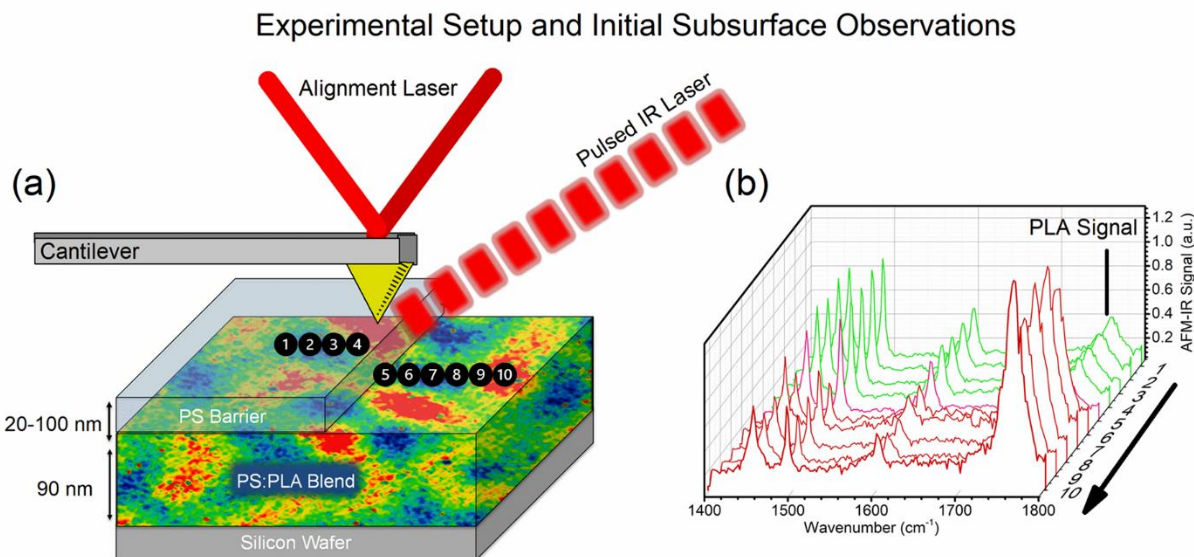

Figure 1. (a) Sample and AFM-IR configuration for bilayer sample measurement. (b) AFM-IR spectrum corresponding with the scan direction indicated by the arrow in Fig. 1a.

depth to which AFM-IR can practically detect subsurface morphology features. This study fills a gap in the current understanding of AFM-IR related to non-destructive nanotomography. Furthermore, it is the first explicit demonstration of control over the depth of characterization in an all-organic system.

RESULTS

Experimental setup and first observations of depth sensitivity

Our approach consists of preparing a polymer blend that phase-separates at the micron-scale to create a recognizable pattern that can be distinguished easily from any noise in the system. We selected PLA and PS for this blend, which strongly phase separate and remain below their glass transition temperature to avoid significant phase-shifting over time. PLA displays a carbonyl absorption peak at 1760 cm^{-1} in the infrared spectrum, which PS does not share. By tuning the IR laser to one of PLA's signature wavenumbers, the PLA phase of the blend will respond while the PS phase will not. Bilayer films were prepared using a continuous bottom layer consisting of a 1:1

blend of PS with PLA and a top barrier layer of PS with carefully-controlled thickness ranging between 0-105 nm. Details about bilayer sample preparation can be found in the experimental section and **Figure S1**. Unless otherwise noted, AFM-IR was used in contact mode exclusively. Pulsed IR laser was tuned to the unique resonant frequency of the carbonyl bond (~1760 cm^{-1}), and laser power was held constant. **Figure 1a** depicts the AFM-IR setup and bilayer sample configuration and **Figure S2** provides the FTIR spectra for both PLA and PS. The AFM-IR was used to probe the interface of the bilayer sample to simultaneously capture the topography of both the PS barrier layer and PLA:PS bottom layer. The distinct phase-separation of the PLA:PS bottom layer could be observed with high contrast through a barrier layer approximately 50 nm thick. 1-D AFM-IR spectra were also collected across the boundary of the two layers. **Figure 1b** depicts ten spectrums collected across the PS/(PLA:PS) boundary. The prominent PLA peak at 1760 cm^{-1} displays strong absorption in the bottom layer and limited absorption across the PS barrier layer. In a less dramatic display, the peak at 1602 cm^{-1}, corresponding to PS's C=C stretching, decreases in intensity as the probe moves away from the PS barrier layer and onto the bottom layer, which contains only 50 % PS content in the blend. This initial finding confirmed that the compositional measurement by AFM-IR is not limited to the top surface of samples, as previously believed.

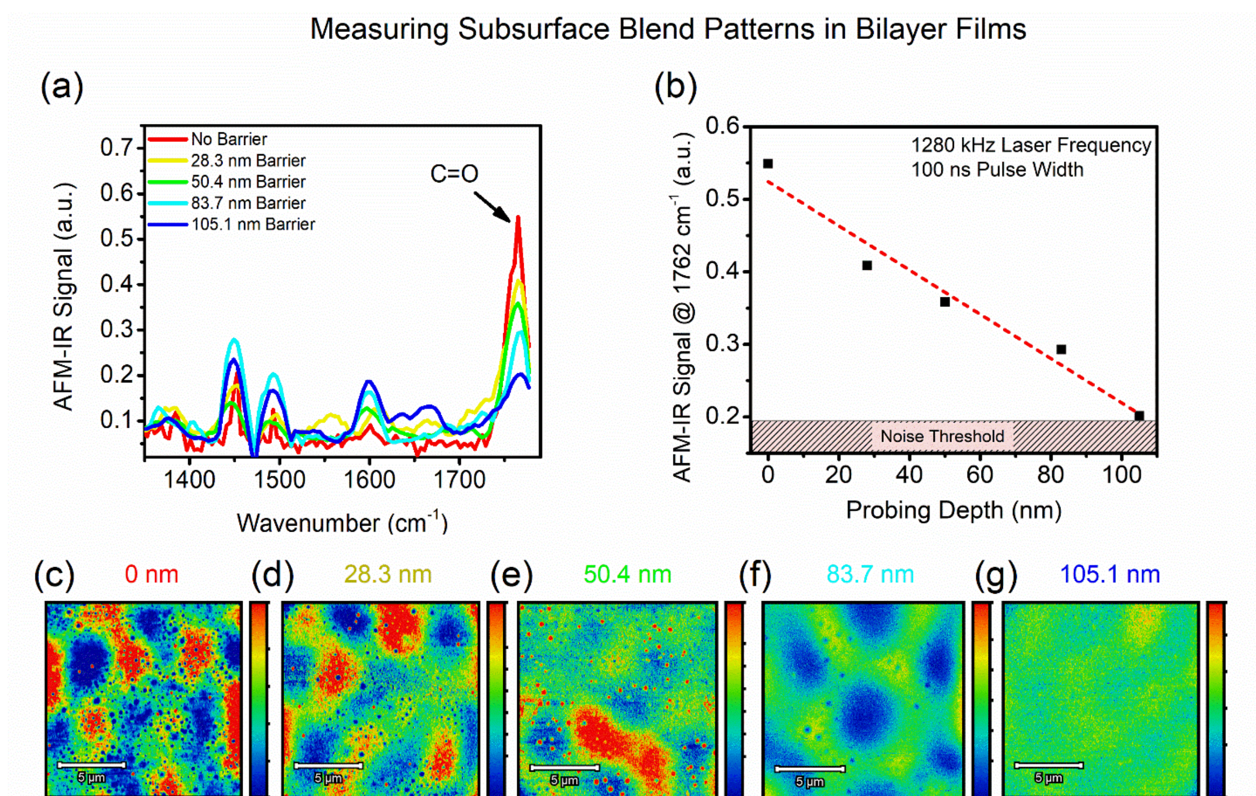

Figure 2. (a) AFM-IR spectra corresponding with measurements collected on bilayer samples of incrementally increasing barrier thickness. (b) AFM-IR signal at 1762 cm^{-1} corresponding to presence of PLA sample as a function of probing depth. AFM-IR imaging collected on bilayer samples with top layer thicknesses of (c) no barrier, (d) 28.3 nm, (e) 50.4 nm, (f) 83.7 nm, and (g) 105.1 nm.

Additional bilayer samples were prepared with top layer thicknesses ranging from 28.3 nm to 105.1 nm with a constant average bottom layer thickness of 88.1 nm. **Figure 2a** depicts AFM-IR spectra collected along the top of the barrier layer with the signature PLA signal at 1762 cm^{-1} decreasing with increasing top layer thickness. The AFM-IR signal at 1762 cm^{-1} was plotted as a function of probing depth (as indicated by top layer thickness) to determine how the signal loss occurred with increasing the distance between the surface and the bottom target layer. **Figure 2b** depicts the decay of the PLA signal as a function of probing depth. The signal loss occurred linearly as top layer thickness increased, further supported by the AFM-IR imaging in **Figures 2c-g** which

highlight the progressive loss of visual contrast between the phase-separated blend pattern of PLA:PS beneath the PS top layer. Interestingly, the relationship between AFM-IR signal and probing depth remained linear in contact mode while displaying exponentially decaying behavior in tapping mode (**Figure S4a**).

Controlling depth sensitivity by altering laser parameters

The AFM-IR may be treated as a closed system with only three significant areas controllable by the commercial user: 1) probe choice, 2) AFM probe scanning parameters, and 3) IR laser parameters. In terms of depth sensitivity, the role of the IR laser is the most logical area to investigate first because it solely influences the thermally driven oscillations in the cantilever caused by the infrared-excited material. Dazzi and coworkers first derived the relationships between photothermal generation and mechanical expansion, which is the foundation for this report.[46,47] From these derived relationships, three main laser properties contribute to the AFM-IR signal (excluding wavelength selected): 1) laser power, 2) laser frequency, and 3) laser pulse width. First, the temperature increases inside the sample that causes oscillation of the cantilever is a direct response to the energy delivered by the infrared laser. The energy produced by the infrared laser is assumed to increase the temperature within a sphere directly beneath the cantilever probe, which causes sample expansion. The heat generated at the point of laser absorption tends to spread out uniformly in all directions, which results in a spherical heat propagation pattern. This is a consequence of the isotropic nature of the heat conduction process in the absence of any external constraints or anisotropic material properties that could lead to preferential heat flow in a specific direction. The expansive change in the radius of the sphere relies heavily on the amount of incident laser energy absorbed by the sample (E_{abs}).[47] Dazzi and coworkers derived the equation for the

relationship between the 1-D expansion of the sample and the incident laser energy absorbed by the sample:

$$\frac{\Delta x}{x} = \alpha \Delta T = \frac{\alpha}{\rho V C_p} E_{abs} \tag{1}$$

Where Δx is the change in sample length, α is the coefficient of thermal expansion, ΔT is the change in sample temperature, ρ is the sample density, V is the sample volume of the irradiated area, C_p is the heat capacity of the sample, and E_{abs} is the absorbed infrared energy of the sample. This equation shows the linear relationship between the absorbed incident laser energy and sample expansion. Therefore, we hypothesize that supplying additional laser power to buried polymeric structures will be sufficient to detect their thermal expansion several nanometers beneath the surface.

Secondly, the relationship between the AFM-IR signal and laser frequency must be investigated. Dazzi and coworkers derived an expression for the AFM-IR signal, which contains multiple contributing factors, as described in the following equation:

$$S_{AFM-IR}(\omega, \gamma) = H_m H_{AFM} H_{opt} H_{th} \frac{Im[n(\gamma)]}{\gamma} \tag{2}$$

Where $S_{AFM-IR}(\omega, \gamma)$ is the AFM-IR signal as a function of the angular frequency (ω) of the cantilever and wavelength of infrared light (γ), H_m, H_{AFM}, H_{opt}, and H_{th} are the mechanical, cantilever, optical, and thermal contributions to the deflection signal.[46] The thermal contribution originates from the infrared radiation produced by the laser and can be expressed by the following equation:

$$H_{th} = \frac{4\pi a^2}{k} \left[\frac{\sin\left(\frac{\omega_n t_p}{2}\right)}{\omega_n} \right] \tag{3}$$

Where a is the radius of the spherical thermal expansion, k is the thermal conductivity of the sample, and ω_n is the angular frequency of the laser at the nth resonance mode of the cantilever. In

this expression, the amplitude of H_{th} is more significant at lower laser frequencies and gradually approaches zero at high ω_n values. Therefore, greater surface sensitivity may be achieved by using higher angular laser frequencies to minimize the thermal contribution to the deflection signal. Likewise, lower angular laser frequencies may yield higher sensitivity to subsurface features.

Lastly, the relationship between the AFM-IR signal and laser pulse width requires investigation. The laser pulse width is a measure of how long the material is irradiated during one ON-cycle of the infrared laser. The relaxation time needed for the sample to recover from the expansion caused by the laser depends on the relaxation time of the sample (t_{relax}) and the duration of the laser pulse (t_p). The total sample relaxation time is given in equation 4[47]:

$$t_{def} = t_p + t_{relax} \quad (4)$$

The relaxation time of the sample (t_{relax}) can be calculated using equation 5:

$$t_{relax} = \frac{\rho C_p}{3k_{th}} R^2 = \frac{R^2}{D} \quad (5)$$

Where k_{th} is the thermal conductivity of the sample, R is the radius of the sphere where the thermal oscillations originate in the sample, and D is the equivalent thermal diffusivity. For situations where $t_{relax} << t_p$, the total expansion time of the sample will primarily depend on the duration of the laser pulse.[47] In contrast, for situations where $t_{relax} >> t_p$, the total expansion time will depend primarily on the relaxation time of the sample. Additionally, the relationship between the laser pulse width and the maximum change in sample temperature (T_{max}) is given by equation 6[46,47]:

$$T_{max} = \frac{P_{abs} t_p}{\rho C V} \quad (6)$$

Therefore, it was hypothesized that the depth of AFM-IR measurements could be controlled by altering the laser pulse width by controlling the temperature generated in the absorbing sample and

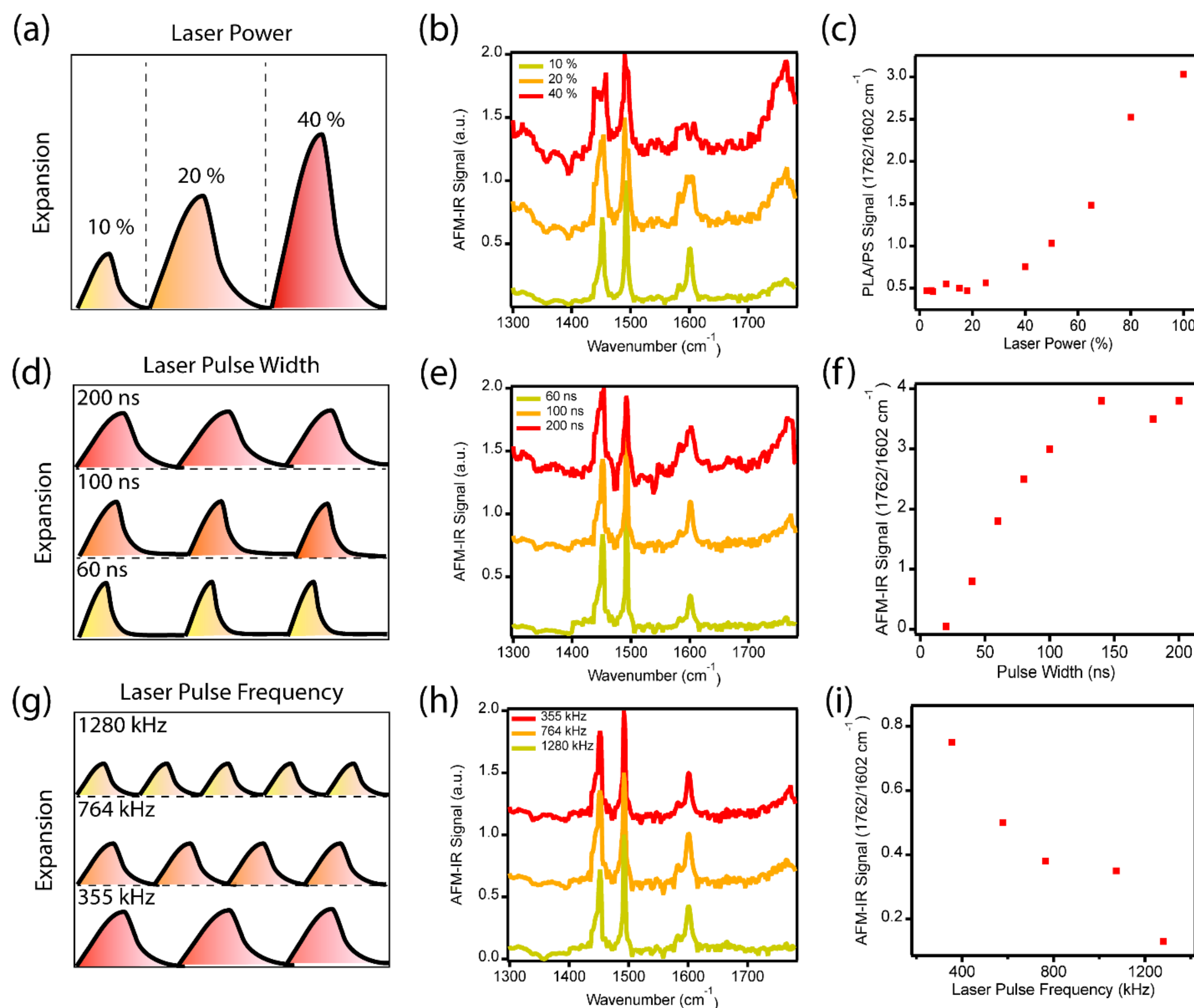

Figure 3. (a) C=O Signal Intensity as a function of percentage laser power. (b) Relationship between thermal expansion of sample as a function of time for incrementally shorter laser pulse widths. (c) Ratio of PLA/PS AFM-IR signal as a function of laser frequency for pulse widths of 60, 100, and 200 ns. AFM-IR spectra collected at different laser frequencies at laser pulse widths of (d) 60 ns, (e) 100 ns, and (f) 200 ns.

the sample illumination time. By controlling the laser pulse width, the dose of energy delivered to the buried polymeric structure can be carefully controlled to enhance or attenuate the thermal oscillations produced within the sample.

It was hypothesized from these relationships that the depth sensitivity of AFM-IR could be controlled to either probe subsurface structures and domains or solely surface morphology in an approach towards surface sensitivity. Three main experimental parameters were investigated to

manipulate the interaction between the laser and target materials: 1) laser power, 2) laser pulse width, and 3) laser pulse frequency. A PS(top)/PLA bilayer sample with a barrier thickness of 18 nm was selected. AFM-IR measurements were acquired in contact mode. The influence of laser properties on depth sensitivity was determined by measuring a PS/PLA bilayer sample using a laser power range from 1-100 % with a maximum average power of 40 mW, a laser frequency ranging from 355-1382 kHz, and using three laser pulse widths of 60, 100, and 200 ns.

First, the influence of laser power on the AFM-IR signal was investigated. **Figure 3a** depicts the projected difference in thermal expansion created using incrementally increasing laser power values. **Figure 3b** depicts the raw AFM-IR spectra for increasing laser power values and indicates an increase in the C=O peak signal located at 1762 cm^{-1} with increasing laser power. Finally, **Figure 3c** depicts the PLA/PS AFM-IR signal (1762/1602 cm^{-1}) measured at incrementally increasing laser power values. This signal ratio remains consistent until reaching 25-40 % laser power, where the ratio began to increase linearly until reaching 100 % laser power. This finding supports the linear relationship between incident laser power and depth sensitivity which can be manipulated to alter the depth of probe. Additionally, the sample was also measured in tapping mode where the AFM-IR signal as a function of laser power increased until reaching an asymptotic limit (**Figure S3a-b**).

Secondly, the influence of laser pulse width on the AFM-IR signal was investigated. **Figure 3d** depicts the projected difference in thermal expansion created using incrementally increasing laser pulse width values. **Figure 3e** depicts the raw AFM-IR spectra for increasing laser pulse width values and indicates an increase in the C=O peak signal located at 1762 cm^{-1} with increasing laser pulse width for three different pulse widths. Lastly, **Figure 3f** depicts the PLA/PS AFM-IR signal response as a function of laser pulse width. As pulse width increased, there was a

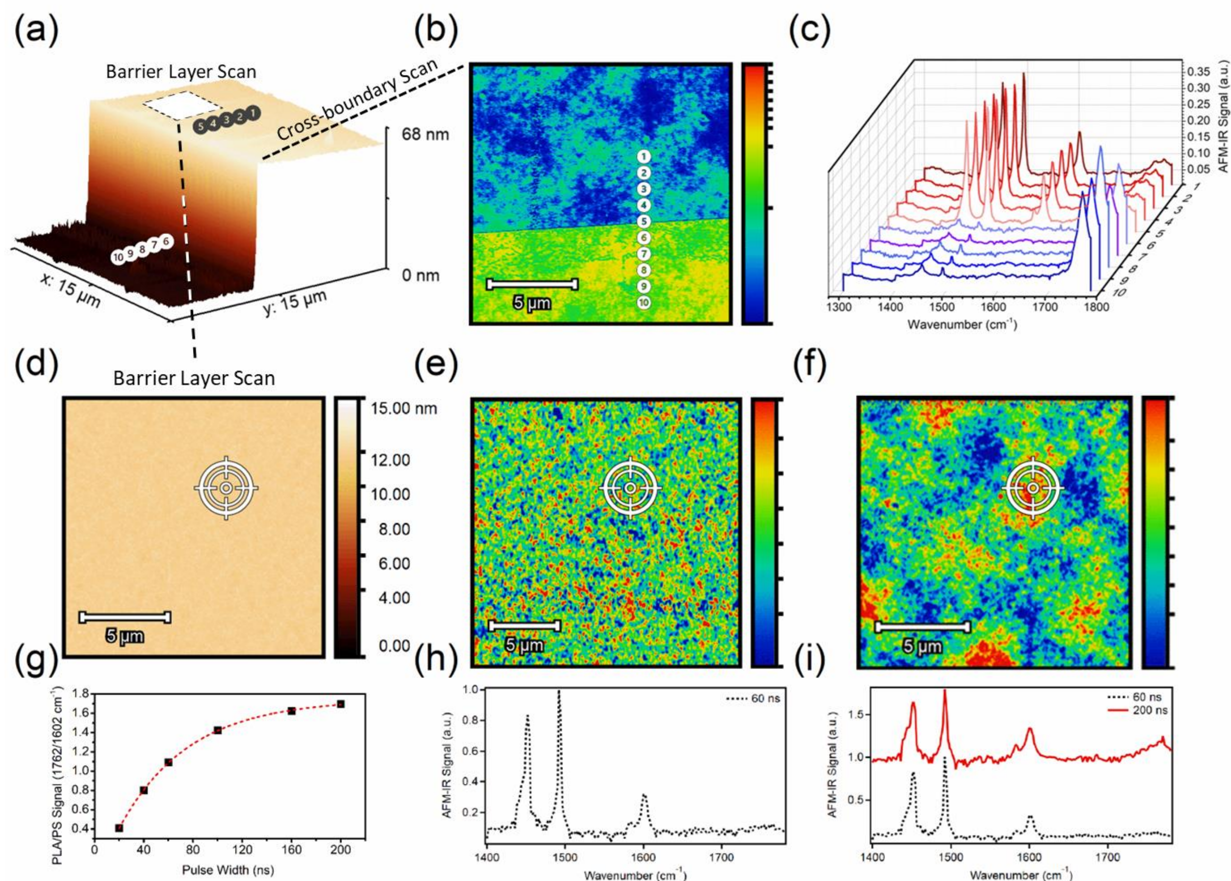

Figure 4. (a) AFM-IR 3-D height image depicting the lateral interface of the bottom layer blend and the top PS barrier layer. (b) IR imaging of the lateral interface collected at the PLA resonance of 1762 cm^{-1}. (c) AFM-IR spectra collected at the locations indicated in (a) and (b). (d) AFM-IR height image of the area covered by the PS top layer. (e) IR imaging of the area covered by the PS barrier layer collected at 1762 cm^{-1} using a laser pulse width of 60 ns. (f) IR imaging of the area covered by the PS barrier layer collected at 1762 cm^{-1} using a laser pulse width of 200 ns. (g) 1-D Plot of the PLA/PS AFM-IR signal as a function of laser pulse width. (h) The 1-D AFM-IR spectra collected using a 60 ns pulse (1074 kHz laser frequency) width corresponding to the scan location indicated in figures 4d-f. (i) The 1-D AFM-IR spectra collected using a 200 ns pulse width corresponding to the scan location indicated in figures 4d-f (collected at 1074 kHz laser frequency).

linear increase in the PLA/PS signal, indicating a linear relationship between depth sensitivity and laser pulse width. Further, In Figure 3f, the AFM-IR signal increases linearly with pulse width until it reaches a pulse width of 150 ns. When the pulse width reaches 150 ns, the AFM-IR signal

plateaus. This suggests that, at identical laser powers, increasing the pulse width beyond 150 ns does not further enhance the thermal expansion in the sample.

Lastly, The influence of laser frequency on depth sensitivity was investigated. **Figure 3g** depicts the projected difference in thermal expansion created using incrementally increasing laser frequency values. The influence of laser frequency on depth sensitivity was investigated by selecting five frequencies between 355 kHz and 1382 kHz and monitoring the ratio of the PLA/PS AFM-IR intensities using laser pulse widths of 60, 100, and 200 ns. The laser pulse frequency is defined as the number of illumination cycles per second for additional clarity. In contrast, the laser pulse width is defined as the duration of each pulse. **Figure 3h** depicts the raw AFM-IR spectra for increasing laser frequency values and indicates a linear decrease in the C=O peak signal located at 1762 cm^{-1} with increasing laser frequency for three different pulse widths. Lastly, **Figure 3i** depicts the PLA/PS AFM-IR signal response as a function of laser frequency. As laser frequency increased, there was a linear decrease in the PLA/PS signal, indicating a inversely-proportional relationship between depth sensitivity and laser frequency. **Figure S4a-b** also depicts the effect of changing pulse frequency and pulse width in tapping mode. While increasing pulse width also showed additional depth sensitivity, there was no effect of changing drive frequency on probing depth.

Demonstration of Controlled Depth Sensitivity

Here, we demonstrate the capability of depth-sensitive AFM-IR to detect buried polymeric structures. For this set of experiments, a bilayer sample was prepared using a bottom layer (89.6 nm thick) composed of a blend of PLA and PS (1:1 v/v), exhibiting microscale phase separation. A top barrier layer (56.1 nm thick) of PS was placed on the blend and imaged by AFM-IR. An AFM height image of the lateral interface between the top and bottom layer is shown in **Figure**

4a. This interfacial area was scanned at the PLA absorbance of 1760 cm^{-1} using a laser power of 25 %, laser frequency of 764 kHz, and a pulse width of 200 ns. The resulting image depicted in **Figure 4b** highlights the presence of PLA in the uncoated bottom layer in high-intensity areas of yellow.

Meanwhile, imaging the area covered by the top barrier layer highlights the presence of PLA in high-intensity areas of green, indicating a reduction in AFM-IR signal due to the presence of the PS barrier. In **Figure 4c**, AFM-IR spectra are collected across the lateral interface in locations depicted in **Figures 4a-b**. The AFM-IR response to the PLA excitation at 1762 cm^{-1} is muted compared to the response observed once the probe contacts the bare PLA:PS blend. Meanwhile, the AFM-IR response to the PS excitation at 1602 cm^{-1} decreases drastically upon crossing the interface due to the reduced PS composition compared to the barrier layer. Rescanning the same bilayer sample on the area covered by the barrier layer resulted in a height image depicting the PS topography with no features indicating the underlying blend phase separation (**Figure 4d**). The targeted area in the image indicates where AFM-IR spectra were collected. The height image of the top layer on top of the bottom layer is in Figure 4e. At this location, the ratio of the PLA/PS signal was monitored as a function of laser pulse width, which produced an asymptotic trendline (Figure 4g). Scanning this area at the PLA resonance of 1762 cm^{-1} using a short laser pulse width of 20 ns resulted in an image depicting no underlying microscale phase separation (Figure 4e). The 1-D AFM-IR spectra collected at the targeted area illustrate the clear presence of PS at 1602 cm^{-1}; however, no response was observed at 1762 cm^{-1} (Figure 4h). Tuning the laser pulse width to 200 ns and rescanning the sample at the same location resulted in the precise imaging of the underlying phase-separated blend with PLA domains highlighted in high-intensity areas of red (Figure 4f). The 1-D AFM-IR spectra collected at this pulse width depicted

an unmistakable PLA signal at 1762 cm^{-1}, indicating that the underlying PLA was sufficiently excited to generate a detectable thermal oscillation (Figure 4i). This observation highlights the control over AFM-IR depth sensitivity by optimizing the properties of the radiation source alone.

CONCLUSION

The influence of infrared laser properties on the depth sensitivity of AFM-IR was investigated by measuring bilayer films containing a bottom target layer and a top barrier layer. Increasing the incident laser power increased the depth sensitivity due to the enhanced thermal vibrations induced by the additional absorbed radiation. Second, adjusting the frequency of pulsation for the infrared laser proved effective in controlling the depth of sensitivity. As bilayer samples were measured, the mathematical ratio of PLA/PS measured using AFM-IR was plotted as a function of the infrared laser frequency. Using higher infrared laser frequencies resulted in a reduced PLA/PS ratio and greater surface sensitivity. The reduced depth sensitivity is caused by tuning the infrared laser frequency to match weaker cantilever resonances, resulting in reduced AFM-IR signal amplitude. Lastly, the laser pulse width was tuned to limit the effective time that the sample was irradiated. By irradiating the sample at shorter time scales, the short thermal relaxation time of the sample allows the sample to relax before the induced thermal vibrations reach the cantilever probe. This effect becomes more apparent as barrier layer thickness increases and heat is dispersed too rapidly to produce a detectable thermal pulse at the cantilever probe/surface interface. With AFM-IR instruments and infrared laser packages now commercially available, the following suggestions offer practical guidance to assess either surface or subsurface features: 1) Improve material contrast by ensuring the feature of interest absorbs infrared light at a unique frequency that is shifted sufficiently away from neighboring absorption bands. This can be achieved either by intentional molecular design or by labeling the feature of interest using an

infrared tag or deuteration. 2) Certain cantilever resonance modes are more sensitive to thermal oscillations than others. Tuning the infrared laser frequency to these cantilever resonance modes results in "resonance-enhanced" AFM-IR measurements. Improve surface sensitivity by tuning the infrared laser frequency to weak cantilever resonance frequencies. Likewise, improve depth sensitivity by tuning the infrared laser frequency to higher cantilever resonance frequencies. 3) Using shorter laser pulse widths produces thermal vibrational responses with shorter lifetimes which may not produce a detectable signal at the cantilever probe/surface interface. Likewise, using a longer laser pulse width is more suitable for detecting subsurface features because a sufficiently strong thermal vibration is created, which may be more readily detected at the cantilever probe/surface interface. Overall, the information found in this study broadens the scope of applications for AFM-IR, including investigations into substructure formations and vertical anisotropy in thin films and composite materials.

METHODS

Materials. All reagents were used as received without further purification unless otherwise noted. Anhydrous toluene was purchased from Fisher Scientific. Polystyrene (M_n: 173,000 g/mol, Đ: 1.06) was purchased from Polymer Source, Inc. Polylactic acid in the form of Ingeo™ Biopolymer 2500HP was purchased from NatureWorks. Molecular weight and polydispersity information is not currently available for this particular grade of polylactic acid.

Bilayer Film Preparation. Bilayer films (top/bottom) of PS/PLA and PS/(PLA:PS) were prepared as follows: bottom layers were deposited by spin-casting 10 mg/mL solutions in toluene at 2,000 RPM onto silicon wafers to produce ~90 nm thick bottom layer films. Top layers with thicknesses ranging between ~28-105 nm were prepared by first depositing 3 % poly(styrenesulfonate) in

water onto a silicon wafer by spin coating and subsequently depositing the top layer material on top of the PSS-coated wafer. Next, the wafer containing the top layer is carefully dipped into a petri dish filled with deionized water until the PSS is dissolved and the top layer remains floating on the surface of the water. The wafer containing the bottom layer is then placed face-down on top of the floating layer and quickly removed from the petri dish. What remains is a silicon wafer containing the top layer overlayed onto the bottom layer with a horizontal offset. Thickness measurements were performed by AFM by placing a controlled scratch across the boundary of the two layers and measuring the vertical distance between the film surface and bare silicon for both the single bottom layer and top double layer.

Atomic Force Microscopy – Infrared Spectroscopy. Spin cast films were measured using a nanoIR3 AFM-IR from Bruker Instruments (Santa Barbara, CA) coupled to a MIRcat-QT™ quantum cascade, mid-infrared laser (frequency range of 917-1700 cm^{-1} and 1900-2230 cm^{-1} using a range of pulse frequencies between 355-1382 kHz). AFM-IR data were collected in contact mode using a gold-coated AFM probe (spring constant (k): 0.07-0.4 N/m and resonant frequency (f_o): 13 ± 4 kHz) sourced from Bruker. The pulsed, mid-IR laser was tuned to frequencies unique to each component as determined by FTIR characterization. Acquired images were flattened using Analysis Studio software. The selected parameters were primarily determined by the limitations of the laser and probe used in the AFM-IR process. First, the laser power levels were chosen based on the laser's adjustable range, which allows for irradiating a sample with power between 1-100%. Second, the laser pulse frequency was determined by the unique resonant frequency of the cantilever probe. Each probe possesses a specific resonant frequency that is used to amplify the thermal expansion signal of the IR-excited area. By inducing thermal expansion at the resonant frequency of the cantilever, the deflection signal is significantly enhanced. Lastly, the laser pulse

width parameters were constrained by the AFM-IR laser's capabilities, which offer a limited range between 20-200 ns.

Author Contributions

N.P. contributed to AFM-IR data acquisition and manuscript preparation. C.C. contributed to sample preparation. X.G. conceived the concept, directed the project, and edited the manuscript. All authors read and commented on the manuscript.

ACKNOWLEDGEMENT

The authors declare no competing financial interest. The authors thank Dr. Anirban Roy and Qichi Hu at Bruker Corporation for helpful discussions. The work presented by the authors was supported by the US Army Engineer Research and Development Center (ERDC) under PE 0603734A, Project T15, Task "Advanced Polymer Development" under ERDC BAA 18-0500 "Multifunctional Materials to Address Military Engineering" executed under Contract No. W912HZ-18-C-0022. Permission to publish was granted by the Director, Geotechnical and Structures Laboratory.

ABBREVIATIONS

AFM-IR, Atomic force microscopy – Infrared spectroscopy; PS, Polystyrene; PLA, Poly(lactic acid); SEM, scanning electron microscopy; TEM, transmission electron microscopy; XPS, X-ray photoelectron spectroscopy; RSoXS, resonant soft X-ray scattering; STXM, scanning transmission X-ray microscopy; KPFM, Kelvin probe force microscopy; SPM, scanning probe microscopy; FTIR, Fourier transform infrared spectroscopy.

REEFERENCES

(1) Wang, M.; Baek, P.; Akbarinejad, A.; Barker, D.; Travas-Sejdic, J. Conjugated Polymers and Composites for Stretchable Organic Electronics. *J. Mater. Chem. C* **2019**, *7* (19), 5534–5552. https://doi.org/10.1039/C9TC00709A.

(2) Yuan, S.; Li, S.; Zhu, J.; Tang, Y. Additive Manufacturing of Polymeric Composites from Material Processing to Structural Design. *Compos. Part B Eng.* **2021**, *219*, 108903. https://doi.org/https://doi.org/10.1016/j.compositesb.2021.108903.

(3) Alam, A.; Zhang, Y.; Kuan, H.-C.; Lee, S.-H.; Ma, J. Polymer Composite Hydrogels Containing Carbon Nanomaterials—Morphology and Mechanical and Functional Performance. *Prog. Polym. Sci.* **2018**, *77*, 1–18. https://doi.org/https://doi.org/10.1016/j.progpolymsci.2017.09.001.

(4) Patel, D. K.; Dutta, S. D.; Lim, K.-T. Nanocellulose-Based Polymer Hybrids and Their Emerging Applications in Biomedical Engineering and Water Purification. *RSC Adv.* **2019**, *9* (33), 19143–19162. https://doi.org/10.1039/C9RA03261D.

(5) Ching, Y. C.; Chuah, C. H.; Ching, K. Y.; Abdullah, L. C.; Rahman, A. *Applications of Thermoplastic-Based Blends*; Elsevier Ltd, 2017. https://doi.org/10.1016/B978-0-08-100408-1.00005-4.

(6) Whitesides, G. M. Nanoscience, Nanotechnology, and Chemistry. *Small* **2005**. https://doi.org/10.1002/smll.200400130.

(7) Goel, M.; Thelakkat, M. Polymer Thermoelectrics: Opportunities and Challenges. *Macromolecules* **2020**, *53* (10), 3632–3642. https://doi.org/10.1021/acs.macromol.9b02453.

(8) Cooke, G.; Evans, I. R.; Skabara, P. J. Functional Organic Materials for Optoelectronic Applications. *J. Mater. Chem. C* **2019**, *7* (22), 6492. https://doi.org/10.1039/c9tc90084e.

(9) Tan, S. T. M.; Quill, T. J.; Moser, M.; LeCroy, G.; Chen, X.; Wu, Y.; Takacs, C. J.; Salleo, A.; Giovannitti, A. Redox-Active Polymers Designed for the Circular Economy of

Energy Storage Devices. *ACS Energy Lett.* **2021**, *6* (10), 3450–3457. https://doi.org/10.1021/acsenergylett.1c01625.

(10) Zarrintaj, P.; Saeb, M. R.; Jafari, S. H.; Mozafari, M. Application of Compatibilized Polymer Blends in Biomedical Fields. In *Compatibilization of Polymer Blends: Micro and Nano Scale Phase Morphologies, Interphase Characterization, and Properties*; 2019. https://doi.org/10.1016/B978-0-12-816006-0.00018-9.

(11) Tropp, J.; Rivnay, J. Design of Biodegradable and Biocompatible Conjugated Polymers for Bioelectronics. *J. Mater. Chem. C* **2021**, *9* (39), 13543–13556. https://doi.org/10.1039/D1TC03600A.

(12) Qian, Z.; Cao, Z.; Galuska, L.; Zhang, S.; Xu, J.; Gu, X. Glass Transition Phenomenon for Conjugated Polymers. *Macromol. Chem. Phys.* **2019**, *220* (11), 1–30. https://doi.org/10.1002/macp.201900062.

(13) Galuska, L. A.; Muckley, E. S.; Cao, Z.; Ehlenberg, D. F.; Qian, Z.; Zhang, S.; Rondeau-Gagné, S.; Phan, M. D.; Ankner, J. F.; Ivanov, I. N.; Gu, X. SMART Transfer Method to Directly Compare the Mechanical Response of Water-Supported and Free-Standing Ultrathin Polymeric Films. *Nat. Commun.* **2021**, *12* (1), 2347. https://doi.org/10.1038/s41467-021-22473-w.

(14) Yuan, Q.; Russell, T. P.; Wang, D. Self-Assembly Behavior of PS-b-P2VP Block Copolymers and Carbon Quantum Dots at Water/Oil Interfaces. *Macromolecules* **2020**, *53* (24), 10981–10987. https://doi.org/10.1021/acs.macromol.0c02422.

(15) Zhang, H.; Clothier, G. K. K.; Guimarães, T. R.; Kita, R.; Zetterlund, P. B.; Okamura, Y. Tuning Phase Separation Morphology in Blend Thin Films Using Well-Defined Linear (Multi)Block Copolymers. *Polymer (Guildf).* **2022**, *240*, 124466. https://doi.org/https://doi.org/10.1016/j.polymer.2021.124466.

(16) Hooda, A.; Goyat, M. S.; Pandey, J. K.; Kumar, A.; Gupta, R. A Review on Fundamentals, Constraints and Fabrication Techniques of Superhydrophobic Coatings. *Prog. Org. Coatings* **2020**, *142*, 105557.

https://doi.org/https://doi.org/10.1016/j.porgcoat.2020.105557.

(17) Polino, G.; Lubrano, C.; Scognamiglio, P.; Mollo, V.; De Martino, S.; Ciccone, G.; Matino, L.; Langella, A.; Netti, P.; Di Carlo, A.; Brunetti, F.; Santoro, F. Synthesis and Characterization of PEDOT-PEGDA Blends for Bioelectronic Applications: Surface Properties and Effects on Cell Morphology. *Flex. Print. Electron.* **2020**, *5* (1), 14012. https://doi.org/10.1088/2058-8585/ab71e1.

(18) Xu, J.; Wu, H.-C.; Mun, J.; Ning, R.; Wang, W.; Wang, G.-J. N.; Nikzad, S.; Yan, H.; Gu, X.; Luo, S.; Zhou, D.; Tok, J. B.-H.; Bao, Z. Tuning Conjugated Polymer Chain Packing for Stretchable Semiconductors. *Adv. Mater.* **2021**, *n/a* (n/a), 2104747. https://doi.org/https://doi.org/10.1002/adma.202104747.

(19) Zheng, Y.; Yu, Z.; Zhang, S.; Kong, X.; Michaels, W.; Wang, W.; Chen, G.; Liu, D.; Lai, J.-C.; Prine, N.; Zhang, W.; Nikzad, S.; Cooper, C. B.; Zhong, D.; Mun, J.; Zhang, Z.; Kang, J.; Tok, J. B.-H.; McCulloch, I.; Qin, J.; Gu, X.; Bao, Z. A Molecular Design Approach towards Elastic and Multifunctional Polymer Electronics. *Nat. Commun.* **2021**, *12* (1), 5701. https://doi.org/10.1038/s41467-021-25719-9.

(20) Inal, S.; Rivnay, J.; Suiu, A.-O.; Malliaras, G. G.; McCulloch, I. Conjugated Polymers in Bioelectronics. *Acc. Chem. Res.* **2018**, *51* (6), 1368–1376. https://doi.org/10.1021/acs.accounts.7b00624.

(21) Xiong, X.; Zhou, Q.; Zhu, Y.; Chen, Y.; Fu, L.; Liu, L.; Yu, N.; Wu, Y.; van Ree, T. In Pursuit of a Dendrite-Free Electrolyte/Electrode Interface on Lithium Metal Anodes: A Minireview. *Energy & Fuels* **2020**, *34* (9), 10503–10512. https://doi.org/10.1021/acs.energyfuels.0c02211.

(22) Nair, J. R.; Imholt, L.; Brunklaus, G.; Winter, M. Lithium Metal Polymer Electrolyte Batteries: Opportunities and Challenges. *Electrochem. Soc. Interface* **2019**, *28* (2), 55–61. https://doi.org/10.1149/2.f05192if.

(23) Mukherjee, S.; Gowen, A. A Review of Recent Trends in Polymer Characterization Using Non-Destructive Vibrational Spectroscopic Modalities and Chemical Imaging. *Anal.*

Chim. Acta **2015**, *895*, 12–34. https://doi.org/10.1016/j.aca.2015.09.006.

(24) Briggs, A.; Kolosov, O. *Acoustic Microscopy: Second Edition*; 2010. https://doi.org/10.1093/acprof:oso/9780199232734.001.0001.

(25) Soliman, M.; Ding, Y.; Tetard, L. Nanoscale Subsurface Imaging. *Journal of Physics Condensed Matter*. 2017. https://doi.org/10.1088/1361-648X/aa5b4a.

(26) Van Tendeloo, G.; Bals, S.; Van Aert, S.; Verbeeck, J.; Van Dyck, D. Advanced Electron Microscopy for Advanced Materials. *Advanced Materials*. 2012. https://doi.org/10.1002/adma.201202107.

(27) Savikhin, V.; Shapiro, D. A.; Gu, X.; Oosterhout, S. D.; Toney, M. F. Ptychography of Organic Thin Films at Soft X-Ray Energies. *Chem. Mater.* **2019**, *31* (13), 4913–4918. https://doi.org/10.1021/acs.chemmater.9b01690.

(28) Chakraborty, I.; Rongpipi, S.; Govindaraju, I.; B, R.; Mal, S. S.; Gomez, E. W.; Gomez, E. D.; Kalita, R. D.; Nath, Y.; Mazumder, N. An Insight into Microscopy and Analytical Techniques for Morphological, Structural, Chemical, and Thermal Characterization of Cellulose. *Microsc. Res. Tech.* **2022**, *85* (5), 1990–2015. https://doi.org/https://doi.org/10.1002/jemt.24057.

(29) Natarajan, B.; Lachman, N.; Lam, T.; Jacobs, D.; Long, C.; Zhao, M.; Wardle, B. L.; Sharma, R.; Liddle, J. A. The Evolution of Carbon Nanotube Network Structure in Unidirectional Nanocomposites Resolved by Quantitative Electron Tomography. *ACS Nano* **2015**. https://doi.org/10.1021/acsnano.5b01044.

(30) Midgley, P. A.; Dunin-Borkowski, R. E. Electron Tomography and Holography in Materials Science. *Nature Materials*. 2009. https://doi.org/10.1038/nmat2406.

(31) Egerton, R. F. *Electron Energy-Loss Spectroscopy in the Electron Microscope*; Second edition. New York : Plenum Press, [1996] ©1996.

(32) Krivanek, O. L.; Chisholm, M. F.; Nicolosi, V.; Pennycook, T. J.; Corbin, G. J.; Dellby, N.; Murfitt, M. F.; Own, C. S.; Szilagyi, Z. S.; Oxley, M. P.; Pantelides, S. T.; Pennycook,

S. J. Atom-by-Atom Structural and Chemical Analysis by Annular Dark-Field Electron Microscopy. *Nature* **2010**, *464* (7288), 571–574. https://doi.org/10.1038/nature08879.

(33) Wi, S.; Shutthanandan, V.; Sivakumar, B. M.; Thevuthasan, S.; Prabhakaran, V.; Roy, S.; Karakoti, A.; Murugesan, V. In Situ X-Ray Photoelectron Spectroscopy Analysis of Electrochemical Interfaces in Battery: Recent Advances and Remaining Challenges. *J. Vac. Sci. Technol. A* **2022**, *40* (1), 10808. https://doi.org/10.1116/6.0001460.

(34) Fadley, C. S. X-Ray Photoelectron Spectroscopy: Progress and Perspectives. *J. Electron Spectros. Relat. Phenomena* **2010**. https://doi.org/10.1016/j.elspec.2010.01.006.

(35) Collins, B. A.; Li, Z.; Tumbleston, J. R.; Gann, E.; Mcneill, C. R.; Ade, H. Absolute Measurement of Domain Composition and Nanoscale Size Distribution Explains Performance in PTB7:PC71bm Solar Cells. *Adv. Energy Mater.* **2013**. https://doi.org/10.1002/aenm.201200377.

(36) Collins, B. A.; Gann, E. Resonant Soft X-Ray Scattering in Polymer Science. *J. Polym. Sci.* **2021**, *n/a* (n/a). https://doi.org/https://doi.org/10.1002/pol.20210414.

(37) Gilchrist, J. B.; Heutz, S.; McComb, D. W. Revealing Structure and Electronic Properties at Organic Interfaces Using TEM. *Curr. Opin. Solid State \& Mater. Sci.* **2017**, *21*, 68–76.

(38) Shapiro, D. A.; Yu, Y.-S.; Tyliszczak, T.; Cabana, J.; Celestre, R.; Chao, W.; Kaznatcheev, K.; Kilcoyne, A. L. D.; Maia, F.; Marchesini, S.; Meng, Y. S.; Warwick, T.; Yang, L. L.; Padmore, H. A. Chemical Composition Mapping with Nanometre Resolution by Soft X-Ray Microscopy. *Nat. Photonics* **2014**, *8* (10), 765–769. https://doi.org/10.1038/nphoton.2014.207.

(39) Hitchcock, A. P. Soft X-Ray Spectromicroscopy and Ptychography. *J. Electron Spectros. Relat. Phenomena* **2015**, *200*, 49–63. https://doi.org/https://doi.org/10.1016/j.elspec.2015.05.013.

(40) Garcia, R.; Gómez, C. J.; Martinez, N. F.; Patil, S.; Dietz, C.; Magerle, R. Identification of Nanoscale Dissipation Processes by Dynamic Atomic Force Microscopy. *Phys. Rev. Lett.* **2006**. https://doi.org/10.1103/PhysRevLett.97.016103.

(41) Schröter, K.; Petzold, A.; Henze, T.; Thurn-Albrecht, T. Quantitative Analysis of Scanning Force Microscopy Data Using Harmonic Models. *Macromolecules* **2009**. https://doi.org/10.1021/ma8024464.

(42) Jespersen, T. S.; Nygard, J. Mapping of Individual Carbon Nanotubes in Polymer/Nanotube Composites Using Electrostatic Force Microscopy. *Appl. Phys. Lett.* **2007**, *90* (18), 15–18. https://doi.org/10.1063/1.2734920.

(43) Cui, Z.; Sun, J.; Landerer, D.; Sprau, C.; Thelen, R.; Colsmann, A.; Hölscher, H.; Ma, W.; Chi, L. Seeing Down to the Bottom: Nondestructive Inspection of All-Polymer Solar Cells by Kelvin Probe Force Microscopy. *Adv. Mater. Interfaces* **2016**. https://doi.org/10.1002/admi.201600446.

(44) Govyadinov, A. A.; Mastel, S.; Golmar, F.; Chuvilin, A.; Carney, P. S.; Hillenbrand, R. Recovery of Permittivity and Depth from Near-Field Data as a Step toward Infrared Nanotomography. *ACS Nano* **2014**, *8* (7), 6911–6921. https://doi.org/10.1021/nn5016314.

(45) Dazzi, A.; Prater, C. B. AFM-IR: Technology and Applications in Nanoscale Infrared Spectroscopy and Chemical Imaging. *Chem. Rev.* **2017**, *117* (7), 5146–5173. https://doi.org/10.1021/acs.chemrev.6b00448.

(46) Dazzi, A.; Glotin, F.; Carminati, R. Theory of Infrared Nanospectroscopy by Photothermal Induced Resonance. *J. Appl. Phys.* **2010**, *107* (12), 124519. https://doi.org/10.1063/1.3429214.

(47) Dazzi, A. *PhotoThermal Induced Resonance. Application to Infrared Spectromicroscopy*; Volz, S., Ed.; Springer Berlin Heidelberg, 2009.